Delft University of Technology

Propeller Aircraft Design Optimization for Climate Impact Reduction

Thijssen, R.; Proesmans, P.; Vos, Roelof

Important note
To cite this publication, please use the final published version (if applicable).
Please check the document version above.

PROPELLER AIRCRAFT DESIGN OPTIMIZATION FOR CLIMATE IMPACT REDUCTION

R. Thijssen[1], P. Proesmans[1] & R. Vos[1]

[1]Delft University of Technology, Kluyverweg 1, 2629HS, Delft, The Netherlands

Abstract

This paper studies the climate impact of propeller aircraft which are optimized for either minimum direct operating costs, minimum fuel mass, or minimum average temperature response (ATR_{100}). The latter parameter provides a measure of the global warming impact of the aircraft design, considering both CO_2 and non-CO_2 effects. We study turboprop-powered aircraft in particular because these offer higher propulsive efficiency than turbofan aircraft at low altitudes and low Mach numbers. The propeller aircraft are designed for medium-range top-level requirements, employing a multidisciplinary design optimization framework. This framework uses a combination of statistical, empirical, and physics-based methods, which are verified using existing engine and aircraft data. For this medium-range design case, a climate impact reduction of 16% can be realized when shifting from the cost design objective to the climate objective. The optimal solutions for the fuel mass and climate objectives are nearly identical as CO_2 and other fuel proportional climate effects are the main contributors. The effects of NO_x and contrails are lower than for the turbofan aircraft due to the lower cruise altitude of the propeller aircraft. Compared to turbofan data, propeller-powered aircraft can achieve a further 33% reduction in climate impact, comparing both climate-optimal designs. This reduction is lessened to 23% when the propeller aircraft is constrained to achieve the same mission block time as the turbofan aircraft. Note that these reductions in ATR_{100} require a propeller efficiency of 88%. Overall, the results show that the utilization of propeller-powered aircraft in the medium-range category can further reduce the climate impact compared to climate-optimal turbofan aircraft designs.

Keywords: Propeller Aircraft Design, MDO, Climate Impact, Global Warming

Nomenclature

Latin Symbols

A	aspect ratio [-]
b	wing span [m]
C	work interaction coefficient [-]
C_L	lift coefficient [-]
C_D	drag coefficient [-]
C_{D_0}	zero-lift drag coefficient [-]
D	diameter [m]
d	distance [m]
EI_i	emission index of species i [kg/kg]
F	thrust force [N]
h	altitude or specific enthalpy [m or J/kg]
m	mass [kg]
$\dot{m}$	mass flow [kg/s]
M	Mach number [-]
P	power [W]

p	pressure [N/m^2]
S	wing surface area [m^2]
T	thrust [kN] or temperature [K]
t_{bl}	block time [hours]
V	velocity [m/s]
W	weight [kN]
$\mathbf{x}$	design vector

Greek Symbols

ΔT	surface temperature change [K]
η_{mech}	Mechanical efficiency [-]
η_{total}	total propulsion efficiency [-]
λ_e	shape factor [-]
Π	compressor ratio [-]
ρ	density [kg/m^3]
τ	enthalpy ratio [-]

Sub- and Superscripts

0	sea-level condition or initial value
0.25	measured at quarter-chord
amb	ambient condition
app	approach condition
eng	engine
s	static condition
t	total condition
tH	high-pressure turbine
tl	low-pressure turbine
TO	take-off condition
$*$	optimal solution

Acronyms

ATR	average temperature response [mK]

DOC	direct operating cost [USD/(seat-nm)]
GEOM	geometry
HPT	high-pressure turbine
LHV	lower heating value of fuel [MJ/kg]
LPT	low-pressure turbine
MTOM	maximum take-off mass [kg]
OEM	operating empty mass [kg]
OPR	overall pressure ratio
RF	radiative forcing [W/m^2]
RPK	revenue passenger kilometer
TIT	turbine inlet temperature [mK]
TLAR	top-level airplane requirement
TSFC	thrust specific fuel consumption [kg/(N s)]
XDSM	extended design structure matrix

1. Introduction

The impact of the aviation industry on global warming has become more and more clear through dedicated research in the last decades [1, 2]. The current aviation industry is estimated to be responsible for 5% of all anthropogenic CO_2 emitted in the world [3]. Comparing that to the 24% anthropogenic CO_2 emitted by the transport industry in total, aviation's contribution might seem insignificant. The commercial aviation market was expected to grow around 3% each year before the Corona pandemic hit the world [4]. This growth is estimated to be even larger when all travel restrictions are lifted in the future [5]. Additionally, pollution near airports can cause severe health problems, and therefore, a reduction in aircraft emissions is of great importance [6]. To tackle the health problems, regulations have been imposed to reduce the landing and take-off (LTO) NO_X emissions. The emissions of water vapor (H_2O) and soot aerosols also impact global warming [7, 8]. Lastly, aircraft induced cloudiness (AIC), if persistent, potentially has a large contribution to global warming which is often neglected [9, 10]. The emissions can be reduced with technological advancements made in the future, however, it seems that the growth of the industry is outpacing these advancements [11]. Therefore, a different approach is needed to reduce the climate impact.

Studies on the reduction of emissions have already been performed. Antoine and Kroo [12], performed an optimization for minimum LTO NO_X emitted, minimum noise, and minimum fuel mass. This is a simple way to compare the climate impact early in the design phase, however, the approach lacks other emission types. The same is true for the research by Henderson et al. [13]. A large number of design variables are used, showing more aircraft design trends for the reduction of the CO_2 emitted. These studies have been improved upon by Dallara Schwartz [8] and Proesmans and Vos [14]. Both studies use core design variables to design medium-range aircraft for minimum climate impact. The climate impact is measured with the average temperature response (ATR), which takes both long-lived and short-lived emissions into account. Additionally, the radiative effects due to AIC are taken into account, which is a great improvement compared to the absolute emissions as the design objective [15].

From the studies by Dallara Schwartz [8] and Proesmans and Vos [14], which focused on turbofan aircraft, it is clear that the climate-optimal turbofan aircraft has a lower cruise Mach number (≈ 0.6) and cruise altitude (≈ 7 km). The combination of the altitude and Mach number reduces the effect of NO_X on the climate and prevents the formation of AIC, specifically persistent contrails. However, this cruise altitude and Mach number result in a less-efficient cruise flight of turbofan aircraft, which increases the contribution due to CO_2. In these cruise conditions, propeller aircraft are known to have a larger propulsive efficiency [16]. Propeller aircraft have been studied thoroughly as part of the AGILE 3.0 project[1]. Different innovative configurations are tested and their performance and climate impact are evaluated. For example, the study of Stingo et al. [17] compares a wing-mounted propeller aircraft with a tail-mounted propeller aircraft. Della Vecchia et al. [18] measure the climate impact of

---

[1]See: https://www.agile-project.eu/

a propeller aircraft using the global warming potential (GWP). However, GWP is not the best metric without sufficient comparison [19]. Besides the traditional turboprop architecture, the contra-rotating open rotor (CROR) has regained interest since its main introduction in the advanced turboprop project by Hager et al. [20]. The regained interest is mainly studied by Guynn et al. [21]. The CROR has high potential but lacks applications in current aircraft design. Therefore, the turboprop layout is often preferred in literature.

Although research has shown that climate-optimal turbofan aircraft fly at cruise conditions where propellers are typically more efficient, it appears that climate-optimal propeller aircraft have not been studied in detail. Therefore, it is of interest to evaluate the climate impact of a medium-range, propeller-powered aircraft. This leads to the following research question: "What are the differences in direct operating costs, mission fuel, and climate impact between an optimized propeller-powered aircraft and a turbofan-powered aircraft optimized for the same objectives and mission?" This research question will yield insight into the performance of propeller and their design. As turbofan data is available, a direct comparison of the values will be made. Next, this study can determine if a propeller aircraft design is a realistic option to reduce the climate impact on medium-range routes.

This document is structured as follows. First, Section 2. discusses the optimization problem including the applied constraints. Subsequently, Section 3. describes the design methods. Then Section 4. focuses on the verification and validation of the methods and Section 5. discusses the results. Lastly, Section 6. provides the conclusions of the research.

2. Optimization Definition & Setup

To answer the research question introduced above, a multidisciplinary design optimization (MDO) problem is defined. This section discusses both the optimization problem and the multidisciplinary structure of the problem. First, Section 2.1 discusses the optimization problem and definition. The optimization constraints and structure are discussed in Sections 2.2 and 2.3, respectively.

2.1 Optimization Definition

A medium-range propeller aircraft is optimized for three different objective functions, namely the mission fuel mass (FM or m_{fuel}), the direct operating costs (DOC), and the average temperature response (ATR_{100}). The combination of the three objectives yields insight into the costs, fuel used, and climate impact of the aircraft, as well as the trade-offs made between them. The same objectives are used by Proesmans and Vos [14] such that a direct comparison with the turbofan data can be made.

The aircraft designed in this study has a high-wing, T-tail configuration powered by two turboprop engines. This configuration best represents the current propeller aircraft in operation. As mentioned before, CROR concepts have potential, but lack applicability in the current aviation market.

To design the aircraft, a short design vector is selected to allow for a sufficiently large design space. In total, there are two airframe design variables, two engine design variables, and two mission design variables. These six design variables are summarized in Table 1 together with their respective bounds. The bounds are chosen such that they allow for technological advancements made in the future. An example of this is the compressor pressure ratio limit of 25, which is relatively high for a turboprop. Still the TP400-D6 Turboprop engine used on the AM 400 has a pressure ratio of 25 [2]. For this reason, it has been chosen as the upper bound. Additionally, the bounds are chosen such that the aircraft design is restricted by constraints rather than the imposed bounds.

2.2 Constraints

The constraints limit aerodynamic, geometric, and performance characteristics of the aircraft. The inequality constraints are not to be exceeded and ensure the aircraft design adheres to the regulations or restrictions. The constraints regarding the airframe structure are the maximum span, the propeller ground clearance, and the propeller fuselage clearance. The maximum span is limited by the airport category. Narrow-body aircraft are often designed for a category C airport [3]. The maximum span for

---

[2]Obtained on 23-11-2021 from `http://www.europrop-int.com/the-tp400-d6/`
[3]Obtained on 13-10-2021 from `https://skybrary.aero/articles/icao-aerodrome-reference-code`

Table 1 – Optimization design variables, including the bounds

Design Variable	Symbol	Variable Type	Lower Bound	Upper Bound
Aspect ratio [-]	A	Airframe	7	17
Wing loading [kN/m^2]	W/S	Airframe	2.0	7.0
Compressor pressure ratio [-]	$\Pi_{\text{compressor}}$	Engine	5	25
Turbine inlet temperature [K]	TIT	Engine	1100	1650
Cruise altitude [km]	h_{cruise}	Mission	3.0	10.0
Cruise Mach number [-]	M_{cruise}	Mission	0.25	0.80

this category is set to 36 m. The propeller ground clearance and propeller fuselage clearance are obtained from regulations. These clearances are set to 18 cm and 35 mm, respectively [22].

The other constraints are the limitation on the turbine inlet temperature (TIT) at take-off, the wing loading, and the cruise lift coefficient. The TIT at take-off is restricted by the engine properties, because the high temperature can damage the high-pressure turbine, limiting the TIT during take-off to 2000 K [23]. The wing loading is restricted by the approach velocity of the aircraft, which depends on the aircraft approach category[4]. This is dependent on the aircraft itself, e.g. 70 m/s for a medium-range aircraft [14]. The maximum cruise lift coefficient is based on the buffet onset of the aircraft ($C_{L,\text{buffet}}$), potentially causing unwanted vibrations. The maximum cruise lift coefficient is purely dependent on the Mach number, as it is expected that little sweep is achieved. The relation is obtained from polynomial analysis based on data from Vos and Farokhi [24]. The polynomial used to calculate the maximum lift coefficient is given in Equation (1).

$$C_{L,\text{buffet}} = -0.3624M^2 - 1.8905M + 2.0536 \tag{1}$$

The combination of the constraints and optimization problem is presented mathematically as follows:

$$
\begin{aligned}
\underset{\mathbf{x}}{\text{minimize}} \quad & F(\mathbf{x}) = \text{ATR}_{100}(\mathbf{x}), \text{DOC}(\mathbf{x}) \text{ or } \text{E}_{\text{fuel}}(\mathbf{x}) \\
\text{subject to} \quad & W/S_{\text{TO}} \leq \frac{1}{2}\rho_0 \left(\frac{V_{\text{app}}}{1.23}\right)^2 C_{L_{\max}}, \\
& b \leq b_{\max} = 36\,\text{m}, \\
& \text{TIT}_{\text{TO}} \leq \text{TIT}_{\text{TO, max}} = 2000\,\text{K}, \\
& C_{L_{\text{cruise}}} \leq \frac{C_{L_{\text{buffet}}}}{1.3}, \\
& d_{\text{prop-fus}} \geq 0.035\,\text{m}, \\
& d_{\text{prop-ground}} \geq 0.18\,\text{m}, \\
& x_i^L \leq x_i \leq x_i^U \qquad\qquad \text{for } i = 1, 2, ..., 6
\end{aligned}
\tag{2}
$$

2.3 Optimization Structure

The structure of the optimization problem described is a multidisciplinary design optimization architecture that consists of several analysis methods combined in order to evaluate the design. The optimization architecture can be divided into the aircraft design convergence loop, the cost and climate analysis modules, and the optimizer. The overview of this architecture is illustrated in the extended design structure matrix (XDSM) in Figure 1.

Three main distinct parts of the XDSM diagram can be distinguished: first, the main optimizer in steps 0-10 provides updates of the design vector. Secondly, the aircraft design convergence loop (steps 1 to 6) ensures each aircraft design is consistent in terms of mass and geometry. Finally, the extra modules, indicated in steps 7 to 9, evaluate the direct operating costs, the climate impact, and the constraints discussed in Section 2.2.

---

[4] Obtained on 2-11-2021 from `https://www.skybrary.aero/index.php/Approach_Speed_Categorisation`
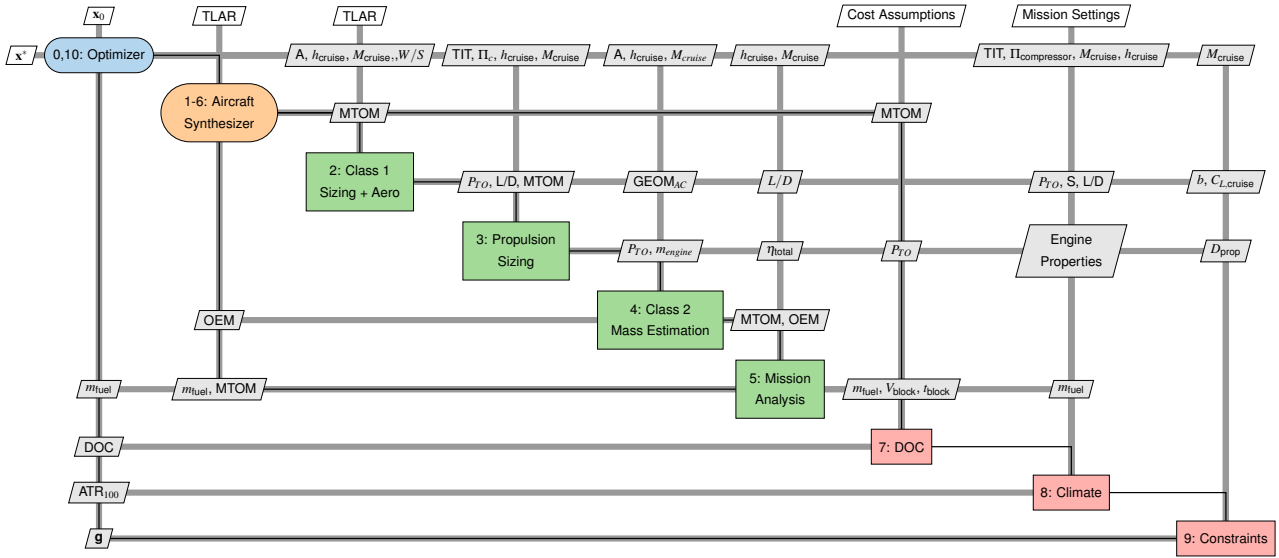
Figure 1 – XDSM diagram of the MDO framework, adapted from Proesmans and Vos [14]

3. Design & Analysis Methods

This section focuses on the modules included in the optimization structure presented in Figure 1. The discussion is divided into three parts: the aircraft design convergence loop (Section 3.1), the climate analysis module (Section 3.2), and the operating cost assessment (Section 3.3).

3.1 Aircraft Design Convergence

The inner convergence loop of the MDO framework designs the aircraft and consists of well-established conceptual design methods. The structure of the design loop is based on the one used in Proesmans and Vos [14], and has been adapted such that a propeller engine and different wing and tail configurations can be used. The focus of this section lies on the newly implemented methods which facilitate the design of propeller aircraft.

3.1.1 Class I Sizing

The design process starts with the statistical estimation of the maximum take-off mass (MTOM) which is the sum of the operative empty mass (OEM), fuel mass, and the required payload mass. The OEM is written in terms of the MTOM, while the fuel mass is obtained from the fuel fraction method which uses the Breguet range and endurance equations [25]. The statistical relation used for the OEM in the first iteration is given in Equation (3).

$$\text{OEM} = 0.563 \cdot \text{MTOM} + 1243.14 \tag{3}$$

Using the estimated MTOM of the aircraft, the wing area and take-off power (P_{TO}) are calculated by using a loading diagram [25]. The loading requirements used are the take-off condition, the cruise condition, the one-engine-inoperative (OEI) climb rate (cr) condition and the OEI climb gradient (cg) condition. The latter requirement is implemented for take-off and landing conditions. While the wing loading is a design variable, the power loading is calculated according to Equation (4). Note that the aerodynamic values of the aircraft in the first iteration are obtained from statistics.

$$W/P = \min \left[W/P_{\text{TO}}(W/S), \quad W/P_{\text{cruise}}(W/S), \quad W/P_{\text{cr,OEI}}(W/S), \quad W/P_{\text{cg,OEI}}(W/S) \right] \tag{4}$$

With the wing area and take-off power known, a conceptual geometry of the aircraft can be constructed. Using statistical relations from Torenbeek [16] and Raymer [25], this geometry is used to update the aerodynamic properties of the aircraft. Assuming a parabolic drag polar, the zero-lift drag coefficient is estimated by splitting the aircraft up in different elements as follows:

$$C_{D_0} = \sum_e^n \left[C_{D,f_e} \cdot \lambda_e \cdot \left(\frac{S_{wet}}{S_{ref}} \right)_e \right] + C_{D,E_I} + C_{D,E_{II}} \cdot \frac{S_{\text{wet}}}{S_{\text{ref}}} \tag{5}$$

5

The flat plate skin friction coefficient (C_{D,f_e}) is estimated for the specific Reynolds. The skin friction co-efficient is then corrected with the compressibility factor and a shape factor (λ_e). The latter is different for different types of aircraft elements, e.g. a cylinder for the fuselage or a wing element for the wing. Lastly, the excrescence drag is added. For the size-independent excrescence drag coefficient (C_{D,E_I}) it is taken as 1.5% of the zero-lift drag coefficient, while the size-dependent coefficient ($C_{D,E_{II}}$) is 3.5% per reference area. The determination of the zero-lift drag coefficient is summarized in Equation (5). Separately, the Oswald efficiency factor is updated with the help of a statistical relation in Obert [26], where the Oswald factor is considered to be a function of the aspect ratio.

3.1.2 Propulsion

The propulsion module characterizes this study, due to the limited consideration of propeller propulsion in aircraft climate impact studies. An accurate module to estimate the performance of the engine is necessary, as it directly impacts the performance of the aircraft. A three-spool engine, similar to the PW127, is modeled as a two-spool engine. We assume that the high-pressure turbine drives the compressor stages, while a low-pressure turbine drives the propeller. This leads to one compressor, a high-pressure turbine (HPT) and a low-pressure turbine (LPT). The latter is the free power turbine that drives the gearbox and propeller. This simplification leads to the two design variables for the engine (Π_c, TIT). We employ the methods of Mattingly et al. [23] for the thermodynamic on- and off-design analysis of the engine. The efficiencies are also obtained from the same book. Additionally, no power off-take or cooling flows are assumed in the current analysis.

The propeller engine analysis makes use of the work interaction coefficient (C), which has a propeller and core component. Equation (6) shows the definition for the work interaction coefficient, where P is the power, η represents the efficiency of the propeller, V is the aircraft velocity, F is the thrust, $\dot{m}_0$ is the air mass flow and h_0 is the free-stream specific enthalpy. The work interaction coefficient is used to calculate the engine properties such as the thrust specific fuel consumption (TSFC) and the thermal and propulsive efficiencies. During both the on-design point (parametric) analysis and the off-design point (performance) analysis, the variable specific heat model by Walsh and Fletcher is used [27].

$$C_{\text{total}} = C_{\text{prop}} + C_{\text{core}} = \frac{P_{\text{prop}} \cdot \eta_{\text{prop}}}{\dot{m}_0 \cdot h_0} + \frac{F_{\text{core}} \cdot V}{\dot{m}_0 \cdot h_0} = \frac{F_{\text{prop}} \cdot V}{\dot{m}_0 \cdot h_0} + \frac{F_{\text{core}} \cdot V}{\dot{m}_0 \cdot h_0} \tag{6}$$

We noticed that the approach from literature is numerically unstable for the performance analysis and that mistakes in the equations are present in both analyses. The former problem is resolved by adding a simple numerical stabilizer. This makes the analysis numerically stable, but also more computationally expensive. The stabilizer uses both the newly calculated exit Mach number ($M_{9,\text{calculated}}$) and the exit Mach number from an earlier iteration ($M_{9,\text{prev}}$) to calculate the new value. The linear proportional gains (k_1, k_2) fasten or slow down the calculation dependent on their values. The implemented numerical stabilizer is shown in Equation (7).

$$M_{9,\text{new}} = k_1 \cdot M_{9,\text{calculated}} + k_2 \cdot M_{9,\text{prev}} \tag{7}$$

The relations in the book for the work interactions coefficients are corrected by deriving the formulas from the power balance and from the definitions. This results in the following equations for the calculation of the work interaction coefficients (Equations (8) and (9)), the thermal and propulsive efficiency (Equations (10) and (11)), and the TSFC (Equation (12)):

$$C_{\text{prop}} = (1+f) \cdot \eta_{\text{gearbox}} \cdot \eta_{\text{prop}} \cdot (\eta_{\text{mech,LPT}} \cdot \tau_{\text{compressor}} \cdot \tau_{\text{inlet}} \cdot \tau_{tH} \cdot (1 - \tau_{tL})) \tag{8}$$

$$C_{\text{core}} = \frac{V_0}{h_{s,0}} \cdot \left[(1+f) \cdot V_9 - V_0 + (1+f) \cdot T_{s,9} \cdot \frac{R_9}{V_9} \cdot \left(1 - \frac{p_{s,0}}{p_{t,9}} \right) \right] \tag{9}$$

$$\eta_{\text{thermal}} = \frac{C_{\text{total}}}{f \cdot \text{LHV}} \cdot h_{s,0} \tag{10}$$

$$\eta_{\text{propulsive}} = \frac{C_{\text{total}} \cdot h_{s,0}}{h_{s,0} \cdot \frac{C_{\text{prop}}}{\eta_{\text{prop}}} + \left[(1+f) \cdot V_9^2 - V_0^2\right]} \qquad (11)$$

$$\text{TSFC} = \frac{f \cdot V_0}{C_{\text{total}} \cdot h_{s,0}} \qquad (12)$$

In the above equations, f is the fuel-to-air ratio, which is the ratio between the fuel mass flow added in the combustor and the air mass flow entering the combustor. The parameter η represents the efficiency of the various components through which the power is transferred from the turbine. The enthalpy ratio over a component is denoted by τ. The parameters T, p, and R are the temperature, pressure, and gas constant, where the subscripts s and t indicate static or total conditions. The subscripts 0 and 9 correspond to the free-stream conditions and the exhaust exit station, respectively.

The result from the parametric and performance analysis helps to determine the size and the mass of the engine. The geometry of both the engine nacelle and the engine is determined using relations obtained from the lecture slides by Vos et al. [28], based on the take-off power of the engine. The same is true for the mass of the engine, where Equation (13) is used [29].

$$m_{\text{engine}} = 10 \cdot P_{\text{TO}}^{0.266} \qquad (13)$$

The propeller diameter is found with a similar relation [30]. Note that the propeller size and the rotations per minute (RPM) effects on the propeller efficiency are taken into account. The propeller efficiency is assumed to be only dependent on the free-stream Mach number [23, 31]. This propeller efficiency is assumed to be 88% in cruise, which is higher than currently achievable values, however, technological advancements are taken into account [25, 29].

3.1.3 Class II Mass Estimation

The Class II mass estimation updates the OEM of the aircraft using methods which are dependent on the aircraft configuration and size. The aircraft is divided into separate structural groups and each contribution to the aircraft weight is estimated separately. Here the weight differences between the design for different objectives due to the different wing, tail, and engine configuration become apparent. For this study, the methods explained in Torenbeek [16] are used.

The difference with the turbofan configuration is that the aircraft has a high-wing and T-tail instead of a low-wing and conventional tail configuration. The high-wing position increases the weight of the wing-fuselage connection by two-thirds [16]. The main landing gear is stowed in the fuselage, and thus a belly fairing is needed, which adds 7% to the fuselage weight. Lastly, the vertical tail needs to be strengthened to accommodate the horizontal tail that is placed on top of the vertical tail.

The OEM is updated, such that a new MTOM can be generated. This updated MTOM is used in the subsequent modules and design iterations.

3.2 Climate Impact Evaluation

The determination of the climate impact is an intricate task and ideally a metric is used that directly measures the future costs and damages caused by the change in the global climate. These metrics do exist, but are highly uncertain and for that reason the previously mentioned ATR metric is used in this study [8]. Note that the 5-step question process from Grewe and Dahlmann [15] is adhered to for the computation of this metric.

To calculate the ATR of a particular aircraft design, a hypothetical fleet scenario is used. The aircraft designed for each objective will be introduced into the market in the year of 2020, to allow for a direct comparison with the climate data from the turbofan aircraft. Each aircraft in the fleet will have a lifetime of 35 years and the maximum productivity (and fleet size) must be reached in the years 2050-2055 [14, 32]. The hypothetical scenario is explained in more detail in Section 5.1.

Equation (14) defines the average temperature response over a given time horizon H, which is set to 100 years in this study. This allows for the full picture of the different climate effects, both short-lived and long-lived. Within Equation (14), $\Delta T(t)$ is the sea level temperature change of the earth at time t.

$$\text{ATR}_H = \frac{1}{H} \int_0^H \Delta T(t)\, dt \qquad (14)$$

For the calculation of the temperature change $\Delta T(t)$ all climate effects (CO_2, NO_X, SO_4, H_2O, soot and contrails) are evaluated using a linearised climate model [14, 33]. The amount of emitted gas is calculated with the help of the emission index (EI), which indicates how much is emitted per kg of fuel burned. For the emitted amount of the various gasses the emission index is overall set to constant. This assumption is true for CO_2 as the EI is independent of the throttle setting. The same is true for sulfate (SO_4) and water vapor (H_2O). Soot however depends on the throttle setting of the engine, but has such a small climate impact relative to the other effects that a constant EI is assumed [33]. The constants emissions are gathered in Table 2.

Table 2 – Emission indices for various emission species

	CO_2	NO_X	H_2O	SO_4	Soot
EI [kg/kg]	3.16	See Equation (15)	1.26	$2.0 \cdot 10^{-4}$	$4.0 \cdot 10^{-5}$

The emission index of NO_X does vary with the engine operation. The impact of NO_X can be quite high for both the cooling effects, which are the methane and ozone reduction in the long term, and warming effect, namely ozone formation in the short term. For this reason the p3-T3 method is used to simulate the throttle setting of the engine, as shown in Equation (15) [8]. This method uses the compressor exit pressure ($p_{t,3}$) and temperature ($T_{t,3}$) to calculate the EI of NO_X.

$$EI_{NO_X} = 0.0986 \cdot \left(\frac{p_{t,3}}{101325} \right)^{0.4} \cdot \exp\left(\frac{T_{t,3}}{194.4} - \frac{H_0}{53.2} \right) \tag{15}$$

Aircraft induced cloudiness (AIC) is not emitted but formed and does have the potential to have a great climate impact. When the right conditions are met, a long and persistent contrail can form, which greatly increases the climate impact for the mission flown. For contrails, the length of the contrail during the mission is determined and the radiative forcing (RF) due to the contrail formation is calculated [14, 34] by multiplying this length with the radiative efficiency. The exact conditions for contrail formation can be found in Schumann [34].

Similar to how the length is summed, the amount of emitted gas for each type is summed and the RF for each type of emission is determined. This RF is normalized such that a doubling in CO_2 concentration corresponds to a normalized RF of one. That normalized RF (RF^*) is integrated in a convolution integral to model the temperature response of the earth. This process is summarized in Figure 2. Note that for NO_X and AIC, a altitude dependent forcing factor is added to model the altitude dependency of these non-CO_2 effects [2, 8].
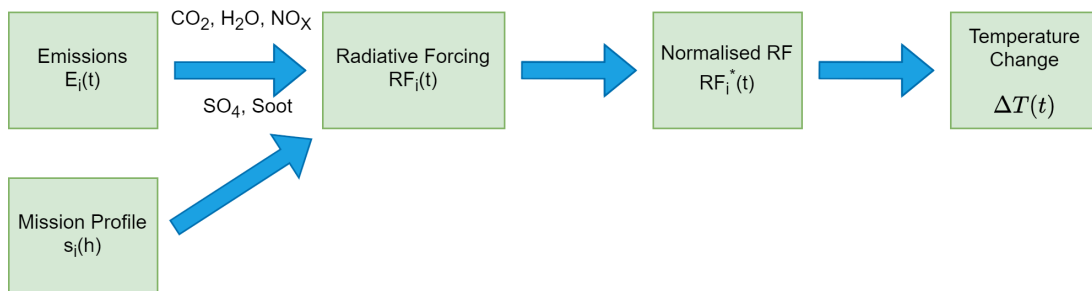

Figure 2 – Workflow to determine the sea-level temperature change, adapted from Dallara Schwartz [35]

3.3 Direct Operating Costs

The cost estimation module estimates the direct operating costs (DOC) of the aircraft. The DOC are calculated based on the methods discussed in Roskam [36]. The DOC are expressed in USD/(seat-nm) to be able to compare it in future studies as well.

The DOC are divided into five categories, which are the flight costs, the maintenance costs, the depreciation costs, operational fees, and the financing costs. Regarding the flight costs, the main contributors are the fuel and oil costs, and the crew costs. For the latter, cabin crew, pilot and co-pilot salaries in the year 2030 have been integrated to take as an average over the next years, using a yearly inflation rate of 2%. For the fuel price the same yearly inflation was used to estimate the kerosene price in the year 2030, which results in $2.71 per US gallon[5].

The maintenance costs, which are dependent on the utilization of the aircraft, consist of the labor for the airframe and engine and the spare material costs. This requires an estimation of the aircraft price, which is done based on the relation from Proesmans and Vos [14] for the medium-range design case. As the engine has a propeller, its price needs to be added to the price of the engine. Equation (16) and Equation (17) show the price estimation for both the engine and propeller, respectively. Note that the inclusion of the 3.32 factor is total inflation rate between 1980 and 2021[6]. Also, the scaling factor (sf) is used to incorporate different engine sizes.

$$P_{\text{engine,2021}} = 3.32 \cdot 2160000 \cdot (0.533 \cdot \text{sf} + 0.467) \tag{16}$$

$$P_{\text{prop,2021}} = 3.32 \cdot 10^{0.7746 + 1.1432 \cdot \log_{10}(P_{\text{TO}})} \tag{17}$$

For the depreciation costs, the calculations are based on a linear depreciation for the airframe, systems and the engine over the next 20 years of the usage of the aircraft. Spare parts are also taken into account. Lastly, the finance costs and the fee costs, which both are assumed as a percentage of the total DOC. The finance costs are assumed 7% of the total DOC, while the fee costs are dependent on the MTOM of the designed aircraft [36].

4. Verification

With the aircraft design methods in place, it is important to ensure the correct workings and implementation. For this, a verification step is performed. Both the propulsion module and the aircraft design convergence verification are discussed in Sections 4.1 and 4.2, respectively.

4.1 Propulsion Module

The propulsion module has to be verified for both the parametric and performance analyses, which are the on-design and off-design point calculations, respectively. The GasTurb 14 program is used for this verification. Additionally, the paper by Dinç [37] is used to verify the parametric analysis. The combination will be sufficient to give insight into whether the module's output is correct.

The parametric analysis in the paper of Dinç [37] considers various mission conditions for the on-design point. The percentage differences between the paper and our model lie between -2% and 5% over all the ten different mission settings which the paper analyses. This difference is seen as acceptable during this conceptual study. Figure 10 shows the results of the ten parametric analyses with the paper by Dinç [37]. The second parametric analysis verification is done with the GasTurb 14 program, of which the input parameters are found Table 3. The result of the on-design verification is observed in the second column of Table 4. The data shows good agreement, as the maximum absolute difference percentage is the TSFC which is only $0.1\,\text{g/(kN\,s)}$, which is accurate for the conceptual design phase considered in this study. Since this is a marginal thrust difference, the parametric analysis is deemed verified.

The performance analysis is quite crucial since it is used much more often during the numerical mission analysis. This analysis is required to assess the climate impact. The engine defined by the variables in the second column of Table 3, is used to determine the off-design point performance of the engine. Two different performance analyses are performed. The results are shown for both analyses in Table 4. For the two different off-design points, the overall percentage difference for the first mission is between -2.9% and 3.2%. For the second mission, the differences lie between -2.4% and +2.2%. This is quite accurate given the conceptual design stage. It is important to note that

---

[5]Obtained from: https://www.indexmundi.com/commodities/?commodity=jet-fuel&months=60
[6]Inflation value obtained on 19-11-2021 at https://www.officialdata.org/us/inflation/1980?amount=1

Table 3 – Input parameters for the Gasturb parametric and the two performance analysis verification

Input Parameter	On-Design	Off-Design #1	Off-Design #2
$\Pi_{\text{compressor}}$ [-]	15	N.A	N.A
M [-]	0.6	0.1	0.3
TIT [K]	1450	1450	1500
h [km]	6.0	0.0	3.0
$p_{s,\text{amb}}$ [kPa]	47.1	101.3	70.1
$T_{s,\text{amb}}$ [K]	249	288	269

the book where the methodology was obtained contained mistakes and the results of this verification indicate that the mistakes were rectified correctly.

Table 4 – Engine performance verification for GasTurb on-design and two off-design points

Parameter	On-Design			Off-Design #1			Off-Design #2		
	Framework	GasTurb	Diff.	Framework	GasTurb	Diff.	Framework	GasTurb	Diff.
$T_{t,5}$ [$10^3 K$]	0.81	0.81	+0.14%	0.87	0.86	+0.93%	0.87	0.86	+0.77%
$p_{t,5}$ [kPa]	265	265	+0.15%	110	110	+0.94%	78.9	78.6	+0.43%
$\dot{m}_0$ [kg/s]	N.A.	N.A.	N.A.	4.52	4.51	+0.13%	3.79	3.79	-0.17%
TSFC [g/(kN s)]	12.7	12.6	+0.78%	4.14	4.01	+3.2%	7.12	6.90	+2.8%
F_{total} [kN]	5.9	5.9	-0.77%	26.0	27.3	+4.8%	13.6	13.9	-2.5%

4.2   Aircraft Design Convergence

The verification of the multidisciplinary aircraft design loop is done by comparing the aircraft geometric aspects and weights of reference aircraft to those predicted by the model. The reference aircraft are the ATR 72-600 and the De Havilland Canada Dash 8-400. The top-level aircraft requirements (TLAR) of both aircraft are summarized in Table 16. For the Dash 8 aircraft, it is important to note that an extra five meters were added to the length of the fuselage cabin to incorporate the extra length in the cabin, which does not seem to be present in other turboprop aircraft [38].

Table 5 shows the overview of the values for both the ATR 72[7] and the Dash 8 [38]. The table shows the three main mass groups, the wing area and fuselage diameter and length for both aircraft. The presented values differ by a maximum of 4.3% for the OEM of the ATR 72, which is deemed within the limits for validation. The values of the Dash 8 are more accurate with a maximum absolute percentage difference of 1.6% in the wing area.

The mission performance of the aircraft is also of interest. The payload-range diagram is used for the verification of the performance. The diagrams are shown in Figure 3 and Figure 4 for the ATR 72 and Dash 8 [38], respectively. Overall, good similarity is achieved, especially for the ATR up until the point where maximum fuel mass is reached. After this point, the slope is underestimated. For the Dash 8 aircraft, the increase in range according to a payload mass reduction is underestimated. The maximum range, however, is quite accurately determined.

---

[7] ATR 72 data: obtained on 21-09-2021 from `https://customer.janes.com/JAWADevelopmentProduction/` `Display/JAWA0440-JAWA`

Table 5 – Validation of ATR-72 and DHC-8 400 parameters with the MDO framework

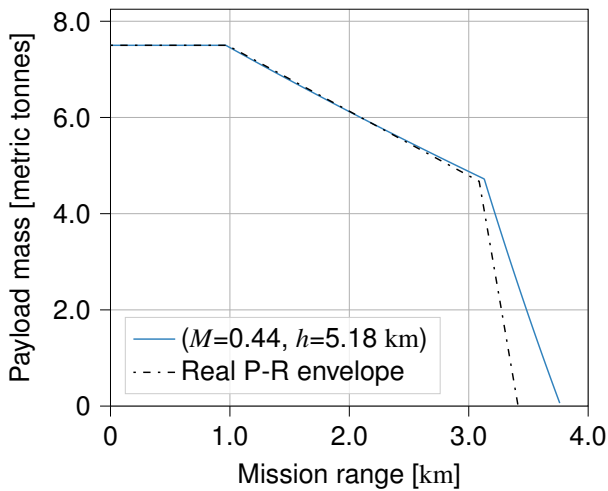| Parameter	ATR 72-600[7]			Dash 8-400 [38]		
	Framework	Reference	Diff.	Framework	Reference	Diff.
MTOM [metric ton]	23.6	2.30	+2.6%	27.5	27.6	-0.3%
OEM [metric ton]	13.9	13.3	+4.3%	17.1	17.1	+0.15%
Fuel Mass [metric ton]	2.2	2.19	+1.5%	2.6	2.61	-1.3%
Wing Area [m^2]	62.7	61.0	+3.5%	62.1	63.1	-1.5%
Fuselage Length [m]	28.0	27.2	+3.1%	33.4	32.8	+1.6%
Fuselage Diameter [m]	2.82	2.9	-2.4%	2.74	2.69	+1.5%

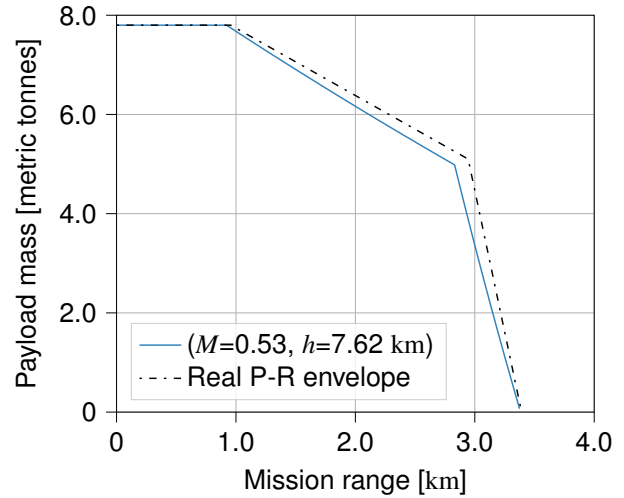Figure 3 – Payload-Range diagram comparison for the ATR 72-600

Figure 4 – Payload-range diagram comparison for the Dash 8-400

5. Results

This section discusses the results of the optimization performed for the three distinct objective functions. In addition, we compare these propeller-powered aircraft to their turbofan counterparts. Throughout the discussion, the objective for which the aircraft is optimized is indicated with an asterisk (*): the fuel mass objective is denoted with FM*, the cost objective with DOC*, and the climate objective with ATR$_{100}^*$.

5.1 Aircraft Design Case Specification

The case of interest in this study is a medium-range, narrow-body aircraft design. This requirements specification allows for a direct comparison with turbofan aircraft that are designed for the same three objectives and TLARs. Table 6 summarizes these requirements. In addition to these TLARs, performance requirements are set which are considered in the selection of the power loading W/P and wing loading W/S. These are for the OEI climb rate, the OEI climb gradient, and the take-off length. The former and latter are 0.762 m/s and 2100 m, respectively. The climb gradient loading requirement is set to 2.1% and 2.4% for take-off and landing segments, respectively.

The direct operating costs, mission fuel, and ATR$_{100}$ objectives are evaluated for one reference mission in the payload-range envelope of the medium-range aircraft. The aircraft transports a payload of 13000 kg over a range of 1852 km (see Table 6). This reference mission is selected from research by Husemann et al. [39], which shows that medium-range aircraft often operate near this point.

The climate impact is assessed for a future hypothetical scenario considering a fleet of only medium-range aircraft. This future fleet acts over a period of 100 years (2020 to 2120) and as-

sumes equal productivity (i.e. equal number of flights) for all optimization objectives. The constant productivity scenario is preferred to a constant fleet scenario since in the latter case the optimizer minimizes the climate impact by reducing the number of flights, making the comparison between objectives unfair. The constant productivity assumption implies that the number of required aircraft can vary with the design objective. This is graphically shown in Figure 9 for the optimized propeller aircraft. The scenario variables are added to Table 6. More information about the future fleet scenarios can be found in Reference [14].

Table 6 – Aircraft design requirements, reference mission data, and future fleet scenario variables for the medium-range aircraft

Parameter [Unit]	Value
Maximum structural payload [kg]	18200
Harmonic Range [km]	3200
Approach speed [$\mathrm{m/s}$]	70
Reference mission payload [kg]	13000
Reference mission range [km]	1852
Yearly utilization [hrs/year]	3900
Productivity$_{2050-2055}$ [RPK per year]	$3.95 \cdot 10^{12}$

5.2 Optimization Results

Employing the above case setup, we optimized the propeller aircraft separately for their operating costs (DOC*), fuel mass (FM*), and climate impact (ATR$_{100}^{*}$). Table 7 shows the optimization results for these three objectives. Each row in the table shows the results for one of the three aircraft. Interestingly, the results for the fuel- and climate-optimal aircraft are nearly identical, even when non-CO_2 effects are considered. This result is different from the turbofan aircraft design solutions, where the two objectives appear to be conflicting. When shifting from the DOC objective to the fuel mass or climate objective, a reduction in ATR$_{100}$ of 15.9% can be obtained. In addition, the mission fuel mass reduces by 15.5%. However, this change in design comes at a penalty of 21% in direct operating costs.

Table 7 – Optimized objective functions for medium-range, propeller-powered aircraft, assuming constant productivity

	Absolute Value			Relative Difference		
Objective	$m_{\mathbf{fuel}}$ [kg]	DOC [$/seat-nm]	ATR$_{100}$ [mK]	$m_{\mathbf{fuel}}$	DOC	ATR$_{100}$
FM*	$4.9 \cdot 10^2$	0.23	7.4	N.A	+21%	+0.0%
DOC*	$5.8 \cdot 10^2$	0.19	8.8	+18%	N.A	+18%
ATR$_{100}^{*}$	$4.9 \cdot 10^2$	0.23	7.4	+0.0%	+21%	N.A

The difference in objective function values is a direct consequence of the chosen design variable values. An overview of the design variables for each optimal design is shown in Table 8. In the overview the overlap between the FM* and ATR$_{100}^{*}$ aircraft is evident. The main differences with the DOC-optimal solution are the cruise altitude and cruise Mach number. The higher Mach number results in lower block time, reducing the crew costs. As a consequence, the cruise altitude is increased to reduce the drag during cruise and maintain a suitable lift-to-drag ratio. The wing loading and aspect ratio are limited for all objectives, by the approach speed and span constraints, respectively. An even higher aspect ratio is desired, but cannot be selected due to the span constraint of 36 m. The

compressor pressure ratio lies on the upper bound. Furthermore, the engine design point is taken at cruise and therefore the higher TIT for the DOC objective is due to the relatively lower throttle setting with the constraining TIT at take-off. This enables a higher TIT in the cruise segment.

Table 8 – Optimal design variables values for the medium-range design case, assuming constant productivity

Design Variable	FM*	DOC*	ATR$^*_{100}$
W/S [kN/m^2]	5.84	5.84	5.84
A [-]	13.9	12.0	13.9
TIT [K]	1412	1564	1415
$\Pi_{compressor}$ [-]	25	25	25
h_{cruise} [km]	4.8	7.5	5.0
M_{cruise} [-]	0.39	0.61	0.40

Table 9 – Aircraft parameters and characteristics for the medium-range design case, assuming constant productivity

Parameter	FM*	DOC*	ATR$^*_{100}$
MTOM [metric ton]	55.2	58.1	55.3
OEM [metric ton]	28.6	30.1	28.5
S [m^2]	92	97	93
W/P [N/W]	0.053	0.043	0.053
TSFC$_{cruise}$ [g/(kN s)]	7.7	10.6	7.6
t_{block} [hrs]	5.2	3.9	5.3
$N_{ac,max}$ [10^3#]	22.0	16.4	22.1
EI$_{NO_X,cruise}$ [kg/kg]	0.011	0.0098	0.011

The aircraft characteristics of the three optimal solutions are summarized in Table 9. The differences between the FM* and ATR$^*_{100}$ are minor, e.g. in the MTOM, OEM and wing area. It is expected that these differences are due to the numerical setup of the aircraft design convergence and optimization. Due to the increase in cruise Mach number, the block time of the DOC-optimal aircraft is reduced significantly, which also reduces the maximum number of aircraft required in the fleet, $N_{ac,max}$. This difference in fleet size is also shown in Figure 9. The top-views geometries are illustrated in Figure 5. The largest differences between the DOC* aircraft and either the FM* or ATR$^*_{100}$ solutions are the span, the propeller diameter, and the nacelle size. However, as all aircraft fly relatively low Mach number, no wing sweep is required. This causes the wing planform to be nearly identical for all objectives.
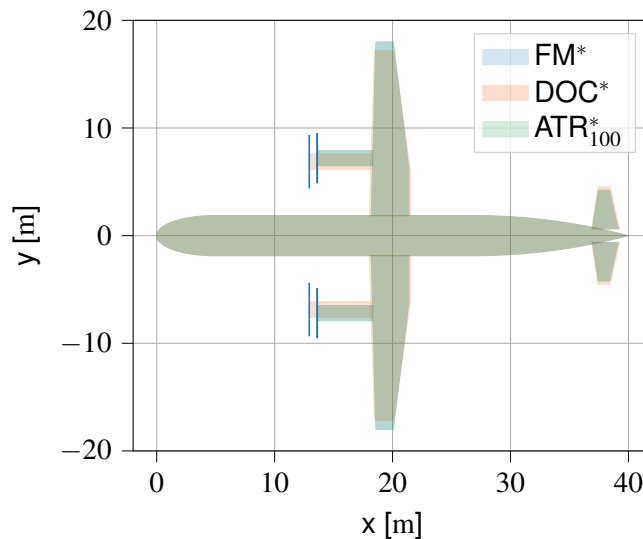

Figure 5 – Optimal aircraft geometry comparison for the medium-range design case, assuming constant productivity

Figure 6 presents the temperature response ΔT of each optimized aircraft design over the 100 years under consideration. It is clear that the fuel- and climate-optimal aircraft have a nearly identical temperature response. Blue and green dots have been added to clarify this overlap. From the shape of the temperature response and the analysis of the contribution of each climate agent to the

ATR_{100}, it is clear that the main contribution for low-flying propeller aircraft follows from fuel proportional emissions and long-lived species, which indicates CO_2 effects are dominant. CO_2 emissions are characterized by a constant emission index and are altitude independent [2, 7]. Also, the water vapor emissions contribute to the climate impact. Although the radiative effect of H_2O varies with altitude, this is not modeled in the current analysis. Nevertheless, due to low cruise altitude, the effects due to H_2O are expected to be short-term and small compared to the contribution of CO_2. Since both CO_2 and H_2O emissions scale linearly with fuel consumption, the higher temperature response of the DOC^* aircraft is noticeable in Figure 6.
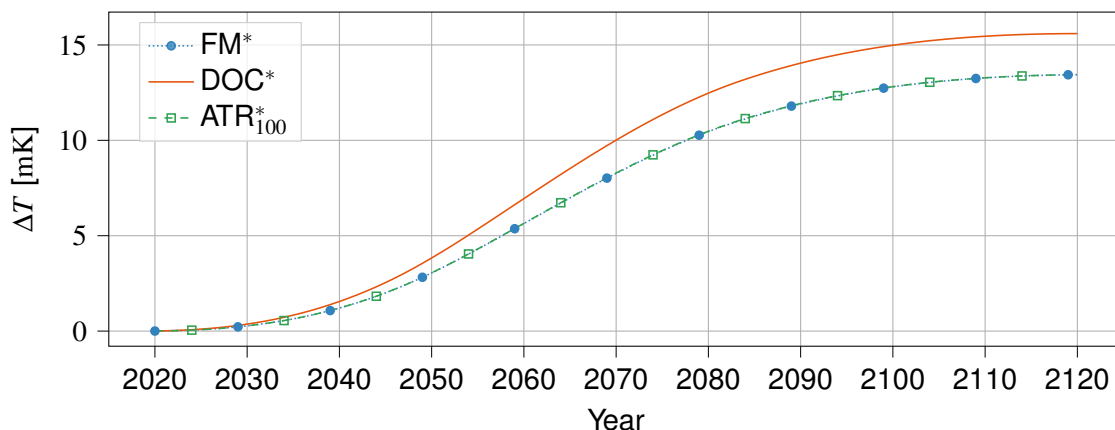

Figure 6 – Sea-level temperature change for the medium-range, turboprop aircraft, assuming constant productivity

The climate impact of NO_X is more complex. The difference in EI_{NO_X} for the objectives is caused by different atmospheric conditions, namely temperature and pressure which vary with cruise altitude. While the total emitted NO_X is similar for the three optimized aircraft, the effects of the DOC-optimal aircraft are more significant due to the altitude forcing factor [35]. This is true for the cooling and warming effects of NO_X.

The last climate effect is the formation of contrails. Under certain conditions, non-persistent contrails may form, but we assume these have no direct influence on the climate. Combining both the knowledge that the NO_X effects are minimal and that persistent contrails do not form in the current case study, this leads to the conclusion that the climate impact is only due to fuel proportional emissions. Hence, in the current optimization structure, minimum fuel mass leads directly to the minimum climate impact as well.

Shifting between the objectives does not only have an impact on the objective values but also on the necessary fleet size as the block time changes with the selective objective function (Table 9). The constant productivity setup results in more aircraft for the FM^* and ATR^*_{100} objectives. The fleet size and constant productivity over the set time horizon of 100 years are illustrated in Figure 9. This results in a maximum fleet size of approximately 22 thousand aircraft for both the FM^* and ATR^*_{100} objectives and 16.4 thousand aircraft for the DOC objective. This is a difference of 5600 aircraft or an increase of 34% between the DOC and the other objectives. To put this into perspective, the productivity rate of the A320 is approximately 540 aircraft per year[8]. Note that the increase in produced aircraft also increases the climate impact, however, the assessment of this impact is out of the scope of this paper.

5.3 Comparison with Turbofan Aircraft

In order to put the results of the optimization into perspective and study which propulsion type is preferred to reduce the global warming impact of aviation, the propeller aircraft are directly compared to their turbofan-powered counterparts. The TLAR, reference mission, and constant productivity scenario are exactly the same as for the propeller aircraft. Table 10 shows the direct comparison of the objective functions between the two types of aircraft. Note that the objectives are now in the columns

---

[8]A320 Production rate: Data obtained on 16-1-2022 from `https://www.airbus.com/en/newsroom/press-releases/2021-01-airbus-updates-production-rates-in-response-to-market-environment`

rather than the rows. From the table, it is clear that generally speaking the turboprop has a lower ATR_{100}, as a reduction of 33% is realized between both ATR_{100}^*-optimized aircraft. This is reduced to 20% when comparing it to the DOC turboprop objective. The cost benefit of the DOC turboprop objective however is unanticipated. The current cost benefit contradicts the current utilization of turbofan aircraft on medium-range routes. For that reason, the current cost prediction for the turboprop is underestimated, by the current assumptions. However, since the range of the reference mission is relatively short (1852 km), the difference in block time and time-related cost between the two aircraft types is limited. In addition, the propeller efficiency of 88% reduces the fuel costs more than current technology allows. For longer ranges, it is expected that the advantage of the faster cruise flight of turbofan aircraft becomes more apparent. Nevertheless, the cost estimation must thus be looked at critically.

Table 10 – Objective function values comparison between the optimal turboprop and turbofan aircraft

Value	Turboprop			Turbofan		
	FM^*	DOC^*	ATR_{100}^*	FM^*	DOC^*	ATR_{100}^*
m_{fuel} [kg]	$4.9 \cdot 10^3$	$5.8 \cdot 10^3$	$4.9 \cdot 10^3$	$7.2 \cdot 10^3$	$7.7 \cdot 10^3$	$7.7 \cdot 10^3$
DOC [$/seat-nm]	0.23	0.19	0.23	0.22	0.20	0.23
ATR_{100} [mK]	7.4	8.8	7.4	26	26	11
t_{block} [hrs]	5.2	3.9	5.3	3.6	3.4	3.9
EI_{NO_X} [kg/kg]	0.011	0.0098	0.011	0.025	0.011	0.017

The difference in block time per mission, as seen in Table 10, has a direct consequence on the fleet size of the objectives between the two aircraft types. This is better illustrated in Figure 7. This figure shows the difference in fleet size between the objectives for both the turboprop (Figure 7a) and the turbofan aircraft (Figure 7b). For example the FM^* or ATR_{100}^* turboprop needs approximately 5500 more aircraft than the ATR_{100}^* turbofan objective. Intuitively, this causes an extra climate impact, but that is out of the scope of this study. As this fleet size discrepancy results in a skewed comparison between the two aircraft types, an extra constraint is added in the next section. A block time constraint can limit the maximum block time to four hours and make the climate impact comparison fairer with the current flight times.

5.4 Block Time Constraint

The addition of the block time constraint partly eliminates the large difference in fleet size eminent between the different objectives. Note that the DOC^* turboprop aircraft remains the same, as the block time per flight is already below four hours. The fuel- and climate-optimal turboprop aircraft change as a result of this constraint.

The new comparison with the turbofan objectives is shown in Table 11. Due to the extra block time constraint, there is a clear increase in the fuel mass and ATR_{100} for both the FM^* and ATR_{100}^* turboprop objectives. For example, the fuel mass for the two objectives is increased from $4.9 \cdot 10^3$ kg to $5.7 \cdot 10^3$ kg, which is still significantly lower than the FM^* turbofan aircraft. Additionally, the costs per flight are lowered, while the ATR_{100} is increased. Generally speaking, the difference between all turboprop objectives becomes smaller and more overlap can be observed between the objective values.

The climate impact benefit observed for the turboprop ATR_{100}^* and FM^* objective is quite optimistic. There are two reasons for this optimistic result: the high propeller efficiency during the cruise segment (88%) assumed and the approach taken for the engine analysis which makes every combination of the compressor pressure ratio and the TIT optimal. A sensitivity analysis is performed in Section 5.5 to study the impact of the assumed propeller efficiency on the results.

When compared to the turbofan objectives the benefit from utilizing turboprop aircraft is significantly smaller. The benefit is reduced to 22%, with a 15% reduction in costs, but, as mentioned, the
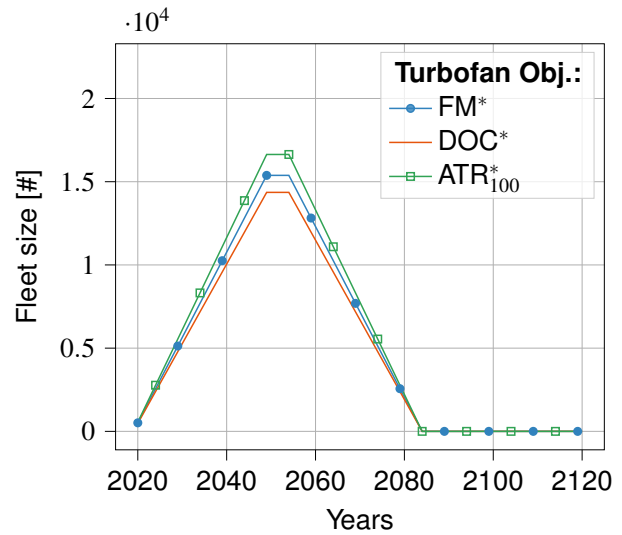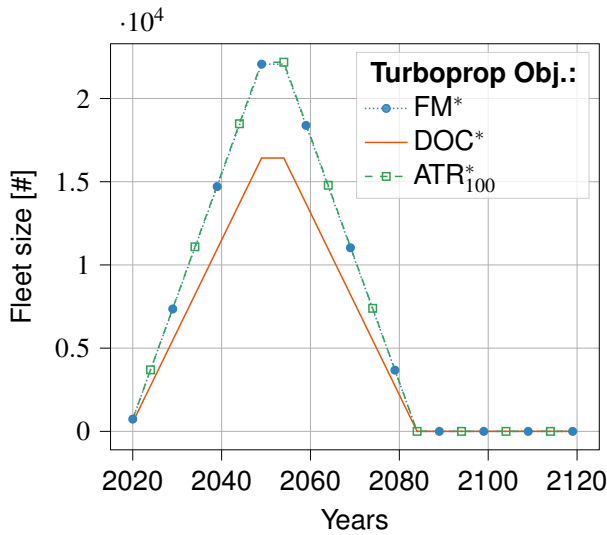
(a) Fleet size over the next 100 years for turboprop objectives assuming constant productivity

(b) Fleet size over the next 100 years for turbofan objectives assuming constant productivity

Figure 7 – Fleet size comparison between the turboprop and turbofan aircraft, assuming constant productivity

Table 11 – Objective function values comparison between the turboprop aircraft with the block time constraint applied, and turbofan aircraft

Value	Turboprop			Turbofan		
	FM*	DOC*	ATR*$_{100}$	FM*	DOC*	ATR*$_{100}$
m_{fuel} [kg]	$5.7 \cdot 10^3$	$5.8 \cdot 10^3$	$5.7 \cdot 10^3$	$7.2 \cdot 10^3$	$7.3 \cdot 10^3$	$7.7 \cdot 10^3$
DOC [$/seat-nm]	0.19	0.19	0.20	0.22	0.20	0.23
ATR$_{100}$ [mK]	8.6	8.8	8.5	26	26	11
t_{block} [hrs]	4.0	3.9	4.0	3.6	3.4	3.9
EI$_{\text{NO}_\text{X},\text{cruise}}$ [kg/kg]	0.0099	0.0098	0.0099	0.025	0.011	0.017

latter must be looked at critically. The difference in maximum fleet size between the two aircraft types is also reduced and is small between the turboprop aircraft and the climate-optimal turbofan aircraft.

The primary changes to the design variables for the FM* and ATR*$_{100}$ design solutions are the cruise altitude and the cruise Mach number. The overview of the design variables is shown in Table 12. For the FM* turboprop objective, the higher cruise Mach number changes the cruise altitude as well. The lower air density is better for the faster velocity. The ATR*$_{100}$ objective has a lower cruise altitude to decrease the effect of NO$_\text{X}$. The overall difference between them is however minimal.

The temperature change over the time horizon of 100 years is compared in Figure 8. The long-term CO$_2$ effects have increased due to the increase in fuel consumption. Regarding NO$_\text{X}$, the increase in cruise altitude results in a higher forcing factor for all NO$_\text{X}$ effects and thus a higher contribution to ATR$_{100}$ per kilogram of fuel. Even though the cruise altitude has increased, persistent contrails do not form at the selected altitude and thus still do not contribute to the temperature increase for the turboprop aircraft.

Table 12 – Optimal design variables for the medium-range design case with the block time constraint applied

Design Variable	FM*	DOC*	ATR$^*_{100}$
W/S [kN/m^2]	5.84	5.84	5.84
A [-]	13.3	12.1	13.1
TIT [K]	1520	1564	1501
$\Pi_{\text{compressor}}$ [-]	25	25	25
h_{cruise} [km]	8.2	7.5	7.2
M_{cruise} [-]	0.60	0.61	0.58
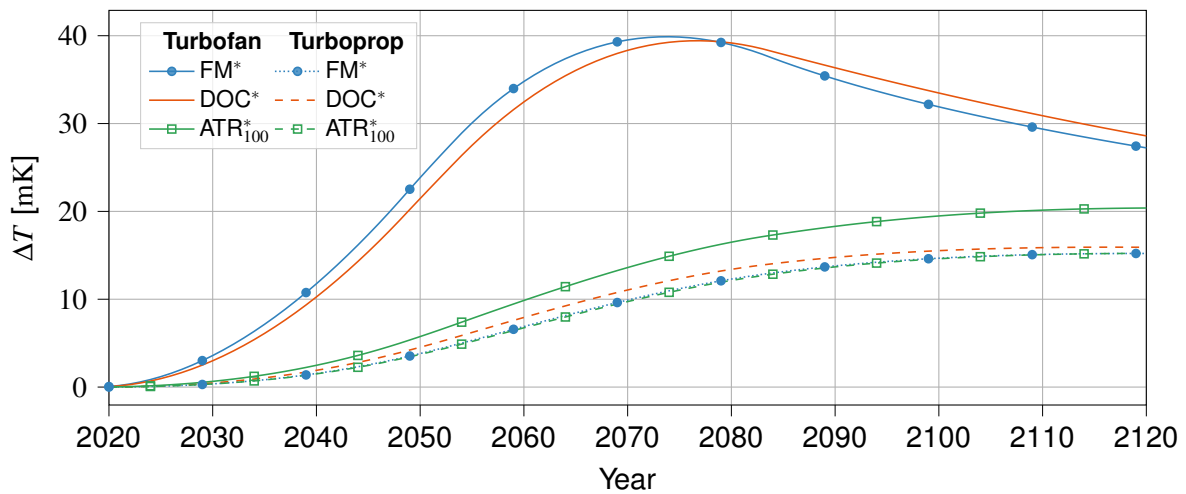
Figure 8 – Sea-level temperature change comparison between the turboprop aircraft with the block time constraint applied, and the turbofan aircraft

5.5   Sensitivity Analysis

The performance of the turboprop aircraft in the previous sections showed an optimistic benefit from utilizing the turboprop aircraft on the medium-range route. To put these results into perspective, a sensitivity analysis is performed in this section. This is done for the standard turboprop aircraft analysis and the analysis with the block time constraint. The maximum propeller efficiency is varied between 70% and 90%. This gives a distinct range and clarifies the impact the propeller efficiency has on the objective values and the design variables.

The impact of the propeller efficiency on the design variables and objective values is shown in Table 13. The impact of the propeller efficiency is clear: as the propeller becomes more efficient, the aircraft performs better in all objectives. The mission fuel mass, the direct operating costs and the climate impact all decrease with increasing propeller efficiency. It is interesting to see that in order to have a comparable climate impact to that of the ATR$^*_{100}$ turbofan aircraft, a propeller efficiency of approximately 75% is required. This gives a threshold that needs to be met to have a lower climate impact than turbofan-powered aircraft.

Considering the design variables shown in Table 13, the differences appear to be limited. The climate optimal cruise conditions are independent of the propeller efficiency and thus are constant. The aspect ratio and the TIT however both increase with an increase in propeller efficiency. The former is caused by the easier conversion from propeller power to thrust and thus a lower throttle setting is needed during the take-off segment. This allows for a higher TIT during the cruise segment. The increase in aspect ratio with increasing propeller efficiency is due to the reduction of wing area in the same trend in combination with the active span constraint.

With the block time constraint applied to the optimization, as shown in Table 14, the same trends

Table 13 – The objective functions and design variables for the ATR^*_{100} turboprop aircraft
for various propeller efficiencies

Parameter	$\eta_{prop} = 0.70$	$\eta_{prop} = 0.75$	$\eta_{prop} = 0.80$	$\eta_{prop} = 0.85$	$\eta_{prop} = 0.88$	$\eta_{prop} = 0.90$
m_{fuel} [kg]	$9.6 \cdot 10^3$	$7.5 \cdot 10^3$	$6.4 \cdot 10^3$	$5.4 \cdot 10^3$	$4.9 \cdot 10^3$	$4.7 \cdot 10^3$
DOC [$/seat-nm]	0.28	0.26	0.25	0.24	0.23	0.22
ATR_{100} [mK]	12	11	9.4	8.0	7.4	7.0
W/S [kN/m^2]	5.8	5.8	5.8	5.8	5.8	5.8
A [-]	11.2	12.1	12.9	13.6	13.9	14.1
TIT [K]	1402	1407	1412	1414	1415	1416
$\Pi_{compressor}$ [-]	25	25	25	25	25	25
h_{cruise} [km]	5.0	5.0	5.0	5.0	5.0	5.0
M_{cruise} [-]	0.40	0.40	0.40	0.40	0.40	0.40

are observed as seen in Table 13. Interestingly, the propeller efficiency threshold to perform better than the turbofan alternative has shifted from 75% to 80%.

Table 14 – The objective functions and design variables for the ATR^*_{100} turboprop aircraft
with the block time constraint applied, for various propeller efficiencies

Paremeter	$\eta_{prop} = 0.70$	$\eta_{prop} = 0.75$	$\eta_{prop} = 0.80$	$\eta_{prop} = 0.85$	$\eta_{prop} = 0.88$	$\eta_{prop} = 0.90$
m_{fuel} [kg]	$11 \cdot 10^3$	$8.7 \cdot 10^3$	$7.3 \cdot 10^3$	$6.2 \cdot 10^3$	$5.7 \cdot 10^3$	$5.3 \cdot 10^3$
DOC [$/seat-nm]	0.25	0.23	0.21	0.20	0.20	0.19
ATR_{100} [mK]	14	12	11	9.3	8.5	8.1
W/S [kN/m^2]	5.8	5.8	5.8	5.8	5.8	5.8
A [-]	10.8	11.7	12.4	12.9	13.2	13.5
TIT [K]	1510	1528	1540	1550	1555	1560
$\Pi_{compressor}$ [-]	25	25	25	25	25	25
h_{cruise} [km]	7.4	7.4	7.4	7.4	7.4	7.4
M_{cruise} [-]	0.59	0.59	0.59	0.59	0.59	0.59

6. Conclusion & Recommendations

The objective of this paper was to investigate the usage of propeller-based propulsion on medium-range aircraft to reduce the climate impact of the aviation industry in the future. Since climate-optimized turbofan aircraft fly at cruise altitude and Mach numbers where turboprop engines typically offer higher propulsive efficiency, both propulsion types are compared. We carried out single-objective optimizations using airframe, engine, and mission design variables. The aircraft were designed and optimized using a multidisciplinary design optimization framework.

The optimization results showed that, for fixed fleet productivity, the climate impact measured by ATR_{100} can be reduced by 16% by shifting from a cost objective to a climate objective for a medium-range propeller aircraft. Interestingly, the same value is obtained when shifting to the fuel mass objective. The climate impact objective and fuel mass objectives were found to be equivalent as the climate impact is mainly caused by CO_2 emissions. Compared to a turbofan aircraft, the result showed a clear reduction of 33% between both aircraft optimized for the climate objective. Compared to the cost-optimal turbofan aircraft, we estimate that the climate-optimal turboprop aircraft can reduce the climate impact by approximately 71%, although uncertainties are present.

Since the climate-optimal turboprop aircraft has a longer block time, the comparison with the turbofan alternative is skewed. When we constrain the mission block time to four hours for the medium-range propeller concept, the reduction potential in ATR_{100} of turboprop aircraft is limited to 23% instead of 33%. In addition, the aforementioned reductions in climate impact require a propeller efficiency of 88%, which is higher than the currently available technology. A sensitivity analysis indicates that a propeller aircraft becomes preferred to the turbofan counterpart when a propeller efficiency of approximately 75% is reached.

This study can be further improved in the future. The first thing is a more advanced propulsion module. The rotations per minute (RPM) and propeller size do not affect the propeller performance in the current model. However, these parameters can strongly influence the propeller efficiency. Regarding future studies, it would be interesting to include a multi-objective optimization for both cost and climate impact objectives. Employing the turboprop and turbofan in a route network can shed a light on how to optimally allocate both aircraft types. Lastly, the use of more advanced climate models is recommended to estimate the climate impact more accurately.

7. Copyright Statement

8. Acknowledgements

9. Contact Author Email Address

The email address of the corresponding author is P.Proesmans@tudelft.nl

References

[1] Lee D. S., Fahey D. W., Forster P. M., Newton P. J., Wit R. C., Lim L. L., Owen B., and Sausen R. Aviation and global climate change in the 21st century. *Atmospheric Environment*, Vol. 43, No. 22-23, pp. 3520–3537, 2009, https://doi.org/10.1016/j.atmosenv.2009.04.024.

[2] Wallace J., and Hobbs P. *Atmospheric Science: An Introductory Survey*. International geophysics series, Elsevier Academic Press, 2006. https://doi.org/10.1016/C2009-0-00034-8.

[3] Lee D. S., Fahey D. W., Skowron A., Allen M., Burkhardt U., Chen Q., Doherty S., Freeman S., Forster P., Fuglestvedt J., Gettelman A., De León R., Lim L., Lund M., Millar R., Owen B., Penner J., Pitari G., Prather M., Sausen R., and Wilcox L. The contribution of global aviation to anthropogenic climate forcing for 2000 to 2018. *Atmospheric Environment*, Vol. 244, pp. 117834, 2021, https://doi.org/10.1016/j.atmosenv.2020.117834.

[4] Airbus. *Global Market Forecast - Cities, Airports and Aircraft 2019-2038*. 5th edition, Airbus S.A.S., Blagnac Cedex, 2019.

[5] Boeing, Commercial market outlook 2020–2039, 2020.

[6] Xue D., Ng K. K. H., and Hsu L.-T. Multi-Objective Flight Altitude Decision Considering Contrails, Fuel Consumption and Flight Time. *Sustainability*, Vol. 12, No. 15, pp. 6253, 2020, https://doi.org/10.3390/su12156253.

[7] Brasseur G., Cox R., Hauglustaine D., Isaksen I., Lelieveld J., Lister D., Sausen R., Schumann U., Wahner A., and Wiesen P. European scientific assessment of the atmospheric effects of aircraft emissions. *Atmospheric Environment*, Vol. 32, No. 13, pp. 2329–2418, 1998, https://doi.org/10.1016/S1352-2310(97)00486-X.

[8] Schwartz E. Aircraft Design for Reduced Climate Impact. Ph.D. thesis, Stanford University, 2011.

[9] Frömming C., Marquart S., Sausen R., and Lee D. The impact of cruise altitude on contrails and related radiative forcing. *Meteorologische Zeitschrift*, Vol. 14, pp. 563–572, 2005, https://doi.org/10.1127/0941-2948/2005/0048.

[10] Hendriks T. Contrail mitigation by means of 4d aircraft trajectory optimisation. *MSc Thesis, Delft University of Technology*, 2015.

[11] Lee J., and Mo J. Analysis of Technological Innovation and Environmental Performance Improvement in Aviation Sector. *International Journal of Environmental Research and Public Health*, Vol. 8, No. 9, pp. 3777–3795, 2011, https://doi.org/10.3390/ijerph8093777.

[12] Antoine N. E., and Kroo I. M. Aircraft Optimization for Minimal Environmental Impact. *Journal of Aircraft*, Vol. 41, No. 4, pp. 790–797, 2004, https://doi.org/10.2514/1.71.

[13] Henderson R. P., Martins J. R. R. A., and Perez R. E. Aircraft conceptual design for optimal environmental performance. *The Aeronautical Journal*, Vol. 116, pp. 1–22, 2012, https://doi.org/10.1017/S000192400000659X.

[14] Proesmans P., and Vos R. Airplane design optimization for minimal global warming impact. *AIAA Scitech 2021 Forum*, Virtual event, AIAA 2021-1297, pp. 1297, 2021, https://doi.org/10.2514/6.2021-1297.

[15] Grewe V., and Dahlmann K. How ambiguous are climate metrics? And are we prepared to assess and compare the climate impact of new air traffic technologies? *Atmospheric Environment*, Vol. 106, pp. 373–374, 2015, https://doi.org/10.1016/j.atmosenv.2015.02.039.

[16] Torenbeek E. *Synthesis of Subsonic Airplane Design*. Springer Netherlands, 1982.

[17] Stingo L., Della Vecchia P., Cerino G., Nicolosi F., and De Marco A. MDO applications to conventional and novel turboprop aircraft within agile European project. *31st Congress of the International Council of the Aeronautical Sciences, ICAS 2018*, Belo Horizonte, pp. 1–10, 2018.

[18] Della Vecchia P., Stingo L., Nicolosi F., De Marco A., Cerino G., Ciampa P. D., Prakasha P. S., Fioriti M., Zhang M., Mirzoyan A., Aigner B., and Charbonnier D. Advanced turboprop multidisciplinary design and optimization within AGILE project. *2018 Aviation Technology, Integration, and Operations Conference*, Reston, Virginia, pp. 1–17, 2018, https://doi.org/10.2514/6.2018-3205.

[19] Fuglestvedt J. S., Berntsen T. K., Godal O., Sausen R., Shine K. P., and Skodvin T. Metrics of climate change: Assessing radiative forcing and emission indices. *Climatic Change*, Vol. 58, No. 3, pp. 267–331, 2003, https://doi.org/10.1023/A:1023905326842.

[20] Hager R., and Vrabel D. *Advanced Turboprop Project*. NASA SP-495, Scientific and Technical Information Division, NASA, 1988.

[21] Guynn M. D., Berton J. J., Haller W. J., Hendricks E. S., and Tong M. T. Performance and Environmental Assessment of an Advanced Aircraft with Open Rotor Propulsion. Tech. rep., 2012. https://doi.org/10.13140/RG.2.1.4847.3687.

[22] European Union Aviation Safety Agency. Certification specifications and acceptable means of compliance for large aeroplanes cs-25: Amendment 26, 2020. URL https://www.easa.europa.eu/document-library/certification-specifications/cs-25-amendment-26-0.

[23] Mattingly J. D., Heiser W. H., and Pratt D. T. *Aircraft Engine Design, Second Edition*. American Institute of Aeronautics and Astronautics, Reston ,VA, 2002. https://doi.org/10.2514/4.861444.

[24] Vos R., and Farokhi S. *Introduction to Transonic Aerodynamics*. Fluid Mechanics and Its Applications, Vol. 110, Springer Netherlands, Dordrecht, 2015. https://doi.org/10.1007/978-94-017-9747-4.

[25] Raymer D. *Aircraft Design: A Conceptual Approach, Sixth Edition*. AIAA education series, American Institute of Aeronautics and Astronautics, Incorporated, 2018.

[26] Obert E. Drag polars of nineteen jet transport aircraft at Mach number M = 0.40 - 0.60. Tech. rep., Fokker, 2013.

[27] Walsh P. P., and Fletcher P. *Gas turbine performance*. 2nd edition, Blackwell Science Ltd, Oxford, 2004.

[28] Vos R., Melkert J., and Zandbergen B., Aerospace Design and Systems Engineering Elements I: Wing and Propulsion System DesignLecture Notes. Delft University of Technology, 2016.

[29] Teeuwen Y. Propeller Design for Conceptual Turboprop Aircraft. *MSc Thesis, Delft University of Technology*, 2017.

[30] Marinus B. G., and Quodbach L. Data and Design Models for Civil Turbopropeller Aircraft. *Journal of Aircraft*, Vol. 57, No. 6, pp. 1252–1267, 2020, https://doi.org/10.2514/1.C035271.

[31] Mattingly J. *Elements of Gas Turbine Propulsion*. AIAA education series, American Institute of Aeronautics and Astronautics, 2005. https://doi.org/https://doi.org/10.2514/4.861789.

[32] Howe S., Kolios A., and Brennan F. Environmental life cycle assessment of commercial passenger jet airliners. *Transportation Research Part D: Transport and Environment*, Vol. 19, pp. 34–41, 2013, https://doi.org/10.1016/j.trd.2012.12.004.

[33] Schwartz E., and Kroo I. Aircraft Design for Reduced Climate Impact. *49th AIAA Aerospace Sciences Meeting including the New Horizons Forum and Aerospace Exposition*, Reston, Virigina, January, 2011, https://doi.org/10.2514/6.2011-265.

[34] Schumann U. Über Bedingungen zur Bildung von Kondensstreifen aus Flugzeugabgasen. *Meteorologische Zeitschrift*, Vol. 5, No. 1, pp. 4–23, 1996, https://doi.org/10.1127/metz/5/1996/4.

[35] Dallara E. S., Kroo I. M., and Waitz I. A. Metric for comparing lifetime average climate impact of aircraft. *AIAA Journal*, Vol. 49, No. 8, pp. 1600–1613, 2011, https://doi.org/10.2514/1.J050763.

[36] Roskam J. *Airplane Design VIII: Airplane Cost Estimation: Design, Development, Manufacturing and Operating*. Airplane Design, DARcorporation, 1990.

[37] Dinç A. Sizing of a turboprop unmanned air vehicle and its propulsion system. *Journal of Thermal Sciences and Technology*, Vol. 35, pp. 53–62, 2015.

[38] Bombardier. Dash 8 series 400, airport planning manual. Tech. rep., Bombardier INC, 2014.

[39] Husemann M., Schäfer K., and Stumpf E. Flexibility within flight operations as an evaluation criterion for preliminary aircraft design. *Journal of Air Transport Management*, Vol. 71, pp. 201–214, 2018, https://doi.org/10.1016/j.jairtraman.2018.04.007.

A   Future Fleet Scenario: Constant Productivity

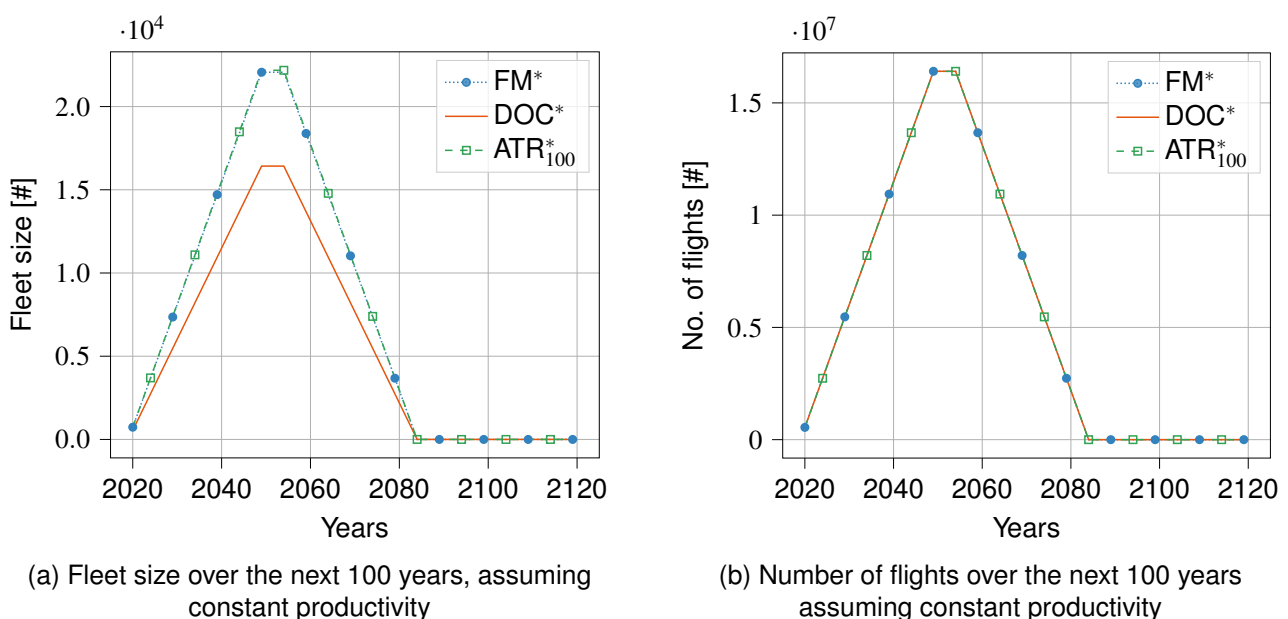Figure 9 shows the change in fleet size required to maintain the same productivity for all objectives.

(a) Fleet size over the next 100 years, assuming constant productivity

(b) Number of flights over the next 100 years assuming constant productivity

Figure 9 – Fleet size and number of flights performed for the medium-range design case, assuming constant productivity

B   Verification Values

The general input parameters for the GasTurb on-design point and off-design point are given in Table 15, while the input parameters for the design convergence loop are provided in Table 16. Additionally, Figure 10 shows the percentage difference the on-design point performance verification with the data from Reference [37].

Table 15 – GasTurb parametric and performance analysis input parameters

Parameter	Value	Parameter	Value
Π_{inlet} [-]	0.99	η_{HPT} [-]	0.85
$\Pi_{\text{combustor}}$ [-]	0.97	$\eta_{\text{mech,HPT}}$ [-]	0.95
Π_{outlet} [-]	0.98	$\eta_{\text{mech,LPT}}$ [-]	0.975
$\eta_{\text{combustor}}$ [-]	0.97	η_{prop} [-]	0.9
η_{LPT} [-]	0.90	LHV [MJ/kg]	43.124
$P_{\text{off-take}}$ [kW]	0.0	Cooling [%]	0.0

Table 16 – Aircraft design convergence verification input parameters

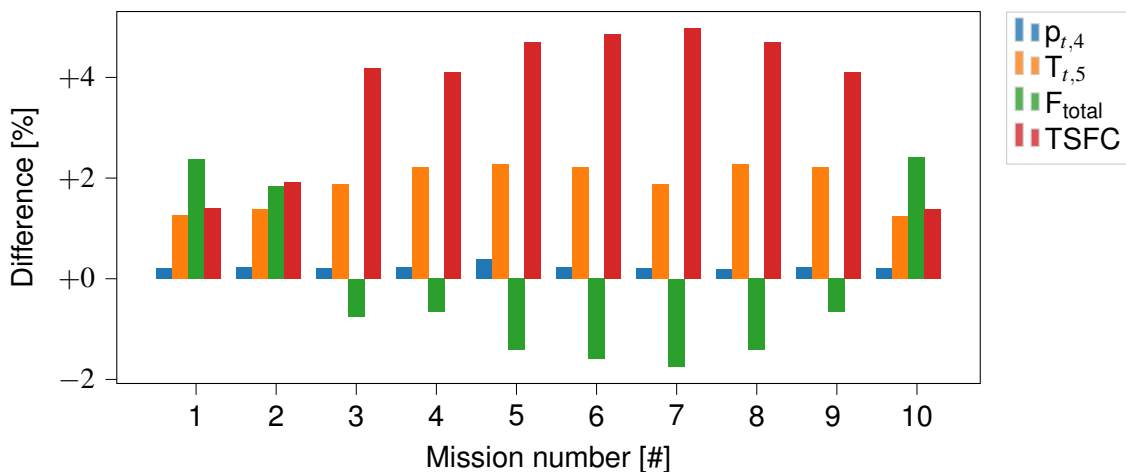| Parameter	ATR 72-600	Dash 8-400
Harmonic Range [km]	987	955
Maximum Structural Payload [kg]	7500	7800
Cruise mach number [-]	0.44	0.53
Cruise altitude [m]	5180	7620
Take-off length [m]	1278	1268
Aspect Ratio [-]	12	12.8
W/S_{TO} [N/m^2]	3697	4351

Figure 10 – Parametric analysis verification of four specific engine parameters with data provided in the paper by Dinç [37]